Received December 11, 2019, accepted December 31, 2019, date of publication January 10, 2020, date of current version January 22, 2020.

Digital Object Identifier 10.1109/ACCESS.2020.2965541

Dynamic Modeling and Experimental Verification of Powered Parafoil With Two Suspending Points

PANLONG TAN, MINGWEI SUN, QINGLIN SUN, AND ZENGQIANG CHEN

College of Artificial Intelligence, Nankai University, Tianjin 300071, China

Corresponding author: Mingwei Sun (smw_sunmingwei@163.com)

This work was supported in part by the National Natural Science Foundation of China under Grant 61973172, Grant 61973175, and Grant 61573197, and in part by the Key Technologies Research and Development Program of Tianjin under Grant 19JCZDJC32800.

ABSTRACT This paper presents the dynamic modeling process of a powered parafoil (PPF). The PPF is composed of parafoil and payload equipped with a propeller. The payload is suspended to the parafoil via two suspending points, therefore the motion of the payload relative to the parafoil must be considered in the dynamic and control study. The proposed model of the PPF is derived from the Lagrangian equations and dynamic constraints with six degree of freedom (DOF) of the parafoil and two DOF of the payload. In the modeling process, the velocity, angular rate and force constraints are introduced and the detailed modeling process is provided. Time-domain response of the PPF under different conditions are calculated and the dynamic characteristics of the PPF are analyzed. A series of simulations are implemented to illustrate the manipulation characteristics. Furthermore, the dynamic model is validated by comparing the simulation results with the experimental data.

INDEX TERMS Powered parafoil, constraint analysis, flexible-wing vehicle, dynamic modeling.

I. INTRODUCTION

Parafoil is a kind of flexible wing aero decelerator which is entirely made of fabric and has a low aspect ratio. This characteristic allows the parafoil to be packed before deployment and be inflated when deployed from a high altitude. The use of parafoil has substantially enhanced airdrop capabilities during the last several decades. Many novel results about the application of the parafoil have been reported in literature [1]–[7].

The concerned powered parafoil (PPF) is composed of parafoil and payload with a propeller equipped on the back of it [8]. The payload is connected to the parafoil via two suspending points to reduce the relative yaw angle. The control inputs for PPF involve lateral brake deflection and longitudinal thrust provided by the propeller. The lateral control is added to the PPF by pulling steering lines on the trailing edge of the parafoil. In the past decades, various control methodologies were applied to the control of the PPF [9]–[15]. The modeling of a PPF is more complicated than a rigid-body aircraft because it is difficult to analyze the internal constraints. In the preliminary research, the connection between the parafoil and the payload is regarded as rigid for simplicity. Therefore, the simplest models of PPF with six degrees of freedom (DOF) [10], [16], [17] or four DOF [18] were established by ignoring the relative motion of the payload. The translational and rotational motions of the whole PPF are investigated based on these models. However, the relative motions affect the actual attitudes of the payload in practice, which then influence the thrust direction. Therefore, a more accurate model should be introduced in the study. A complicated model with nine DOF is proposed by adding three rotational DOF of the payload to the six DOF model of the parafoil [8], [19]–[21]. However, this model is only applicable to parafoil vehicles with only one suspending point between the paraloil and the payload.

The deformation about the roll axis of the PPF with two suspending points is generally very small and can be ignored. Therefore, the dynamics of this type of PPF can be described by an eight DOF model. A nonlinear model with eight DOF was proposed in [22], where the moment about the yaw axis was elaborately modeled. The deformation of the parafoil due to deflection was also taken into account. In [23], flight control of a powered paraglider was described and experimental results were compared with the proposed model, however without theoretical analysis of the motion characteristics.

The associate editor coordinating the review of this manuscript and approving it for publication was Rosario Pecora.

Ref. [24] developed an eight-DOF equations of motion based on analytical mechanics with fewer differentiations than the Lagrangian approach, and the validity of the proposed model was only verified through simulation rather than comparing the simulation with flight test. By eliminating the coupling effects between parafoil and payload, Ref. [25] and [26] established an auxiliary matrix to simplify the modeling process.

In this paper, the detailed derivation of the model of the PPF with eight DOF is presented. The model consists of six DOF of the parafoil and two DOF of the payload. A spring and damper model is utilized to model rotational constraints [25]. In addition, internal forces and moments, which are applicable to the PPF design, are considered as states. This model is available for simulating the unmanned PPF and the numerical simulations are carried out to illustrate the characteristics of the PPF. The results are further compared with experimental data.

The remaining parts of the paper are organized as follows: In section II, the modeling problem is formulated. In section III, the detailed description of the constraints is presented. Then we present the simulation analysis in section IV. In section V, the simulation results are compared with the experimental data, which validates the dynamic model. The concluding remarks are presented in section VI.

II. MOTION EQUATIONS

A practical PPF is shown in Fig. 1. In this paper, we address the modeling problem of the PPF. Several reasonable hypothesis are described as follows [26].

1) The parafoil keeps its aerodynamic structure unchanged when inflated;
2) The center of gravity (CG) of the parafoil is just the aerodynamic pressure center;
3) The lift of payload is ignored, and we only consider its aerodynamic drag;
4) The ground is a flat plane.

FIGURE 1. Powered parafoil.

A. COORDINATE CONFIGURATION

To facilitate the analysis, three main coordinate systems are established, including geodetic coordinate system (inertial coordinate system) Σ_I, parafoil-fixed coordinate system Σ_c and payload-fixed coordinate system Σ_p. These coordinate systems are fixed to a fixed point at the ground, the CG of the parafoil O_c and the CG of the payload O_p, respectively. In addition, two auxiliary coordinate systems, the rigging coordinate system Σ_r and wind coordinate system Σ_w, are established to calculate aerodynamic forces of the parafoil.

As shown in Fig. 2, the axis directions of the coordinate systems are described as follows. The inertial coordinate system Σ_I is defined as $O_I x_I y_I z_I$. The positive direction of z_I-axis is taken downward. The x_I-axis and y_I-axis are properly chosen to ensure that the $O_I x_I y_I$-plane is horizontal. To simplify the simulation of the PPF, the origin of Σ_I is selected at the initial position of CG of the parafoil. The positive direction of x_I-axis is appropriately chosen in the direction of North. The parafoil-fixed coordinate system Σ_c is defined as $O_c x_c y_c z_c$. The z_c-axis is chosen in the direction from O_c to C_m, where C_m is the middle point of the two suspending points. The x_c-axis is in the symmetry plane of the parafoil and is perpendicular to z_c-axis. The y_c-axis is defined so that Σ_c forms a right-hand coordinate system. The payload-fixed coordinate system Σ_p is defined as $O_p x_p y_p z_p$ with the assumption that the payload is symmetric. The x_p-axis is chosen in the direction of the thrust. The z_p-axis is perpendicular to x_p-axis and is taken downward. The Σ_p is also a right-hand coordinate system while the y_p-axis is taken rightward and is perpendicular to the $O_p x_p z_p$-plane. The axes of the parafoil-fixed coordinate system are parallel to those of the payload-fixed coordinate system when the relative attitude between the parafoil and the payload is zero.

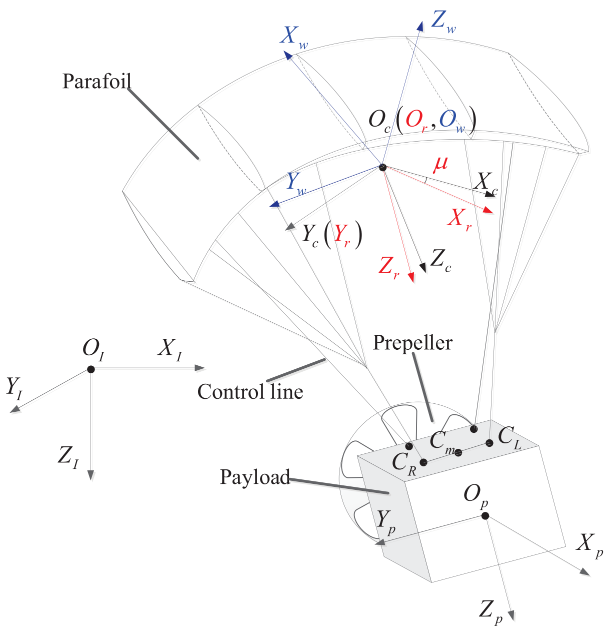

FIGURE 2. Coordinate systems.

Auxiliary coordinate system Σ_r is obtained by rotating Σ_c around the y_c-axis by μ, which indicates the rigging angle. The Σ_r is defined as $O_r x_r y_r z_r$ and the x_r-axis is parallel to the bottom surface of the parafoil. The origin of the wind coordinate system Σ_w is the CG of the parafoil and is defined as $O_w x_w y_w z_w$. The x_w-axis is chosen in the direction of the airflow, which is defined by the airspeed of the parafoil. This makes the Σ_w a dynamic coordinate. The z_w-axis is in the symmetry plane of the parafoil and is perpendicular to the $O_w x_w y_w$-plane.

All the coordinate systems except Σ_I are determined by Eulerian angles, including roll angle ζ, pitch angle θ and yaw angle ψ about Σ_I. The transformation from Σ_I to the related coordinate system is determined by the transformation matrix

$$T_{I-*} = \begin{bmatrix} c_\theta c_\psi & c_\theta s_\psi & -s_\theta \\ s_\zeta s_\theta c_\psi - c_\zeta s_\psi & s_\zeta s_\theta s_\psi + c_\zeta c_\psi & s_\psi c_\theta \\ c_\zeta s_\theta c_\psi + s_\zeta s_\psi & c_\zeta s_\theta s_\psi - s_\zeta c_\psi & c_\psi c_\theta \end{bmatrix} \quad (1)$$

wherein for arbitrary angle α, $\sin\alpha \equiv s_\alpha$, $\cos\alpha \equiv c_\alpha$.

B. MOTION EQUATIONS OF THE PAYLOAD

The payload has translational motion and rotational motion with respect to the force and moment acting on it. For simplicity, the payload is assumed to be rigid in the modeling process.

The forces acting on the payload are gravity $\mathbf{F}_p^G$, aerodynamic force $\mathbf{F}_p^a$, tension of suspension lines $\mathbf{F}_p^{te}$ and the thrust provided by the propeller $\mathbf{F}_p^{th}$, which are described in Σ_p. The action points of the gravity, thrust and aerodynamic force are the CG of the payload for its regular shape, and thus the moments of the three in Σ_p are ignored. Therefore, the basic equations of motion for the payload can be obtained by applying the Lagrange approach. The most general form of these equations in Σ_p are

$$\begin{aligned} &\frac{\partial \mathbf{P}_p}{\partial t} + \omega_p \times \mathbf{M}_p = \mathbf{F}_p^a + F\mathbf{F}_p^G + \mathbf{F}_p^{th} + \mathbf{F}_p^{te} \\ &\frac{\partial \mathbf{H}_p}{\partial t} + \mathbf{V}_p \times \mathbf{P}_p + \omega_p \times \mathbf{H}_p = \mathbf{M}_p^{te} \end{aligned} \quad (2)$$

where $\mathbf{P}$ and $\mathbf{H}$ are momentum and moment of momentum, respectively. $\mathbf{V}_p = \begin{bmatrix} u_p\ v_p\ w_p \end{bmatrix}^T$ and $\omega_p = \begin{bmatrix} p_p\ q_q\ r_p \end{bmatrix}^T$ denote the velocity and angular rate of the payload, respectively, and the superscript T here is the transpose symbol. The subscript p means that the vector is in Σ_p. The superscripts a, G, te and th represent aerodynamic force, gravity, tension of suspension lines and thrust, respectively. $\mathbf{P}_p$ and $\mathbf{H}_p$ are defined as

$$\begin{cases} \mathbf{P}_p = m_p \mathbf{V}_p \\ \mathbf{H}_p = J_p \omega_p \end{cases} \quad (3)$$

where J_p is the matrix of moment of inertia.

Let $T_{I-p}\left(\zeta_p\ \theta_p\ \psi_p\right)$ be the transformation matrix from Σ_I to Σ_p, then the gravity is expressed as $\mathbf{F}_p^G = T_{I-p}^T \left[0\ 0\ m_p g\right]^T$, where m_p is the mass of payload and g is the gravitational acceleration. The aerodynamic lift of the payload can be ignored for its aerodynamic shape. Therefore, $\mathbf{F}_p^a$ is just the aerodynamic drag and can be defined as

$$\mathbf{F}_p^a = -0.5\rho \left|\mathbf{V}_p\right| S_p C_{D_p} \mathbf{V}_p \quad (4)$$

where ρ, C_{Dp} and S_p are the air density, the drag coefficient and the characteristic area of the payload, respectively.

It is assumed that the payload is linked to the parafoil via two suspending points, C_R and C_L. Thus, $\mathbf{F}_p^{te}$ is defined as $\mathbf{F}_p^{te} = \mathbf{F}_{pR}^{te} + \mathbf{F}_{pL}^{te}$ wherein $\mathbf{F}_{pR}^{te}$ and $\mathbf{F}_{pL}^{te}$ are the tensions acting at C_R and C_L, respectively. Let l_p and l be the distance from C_m to O_p and C_m to C_R, respectively. Then, the distance between C_m and C_L is also l. The moment produced by suspension lines is given as

$$\mathbf{M}_p^{te} = \mathbf{L}_{pR} \times \mathbf{F}_{pR}^{te} + \mathbf{L}_{pL} \times \mathbf{F}_{pL}^{te} \quad (5)$$

where $\mathbf{L}_{pR} = \begin{bmatrix} 0\ l\ -l_p \end{bmatrix}^T$ and $\mathbf{L}_{pL} = \begin{bmatrix} 0\ -l\ -l_p \end{bmatrix}^T$ are the positions of C_L and C_R in Σ_p, respectively. Substituting $\mathbf{L}_{pR}$ and $\mathbf{L}_{pL}$ into Eq. (5) yields

$$\begin{aligned} \mathbf{M}_p^{te} &= \left(\begin{bmatrix} 0 \\ l \\ 0 \end{bmatrix} - \begin{bmatrix} 0 \\ 0 \\ l_p \end{bmatrix}\right) \times \mathbf{F}_{pR}^{te} \\ &\quad + \left(-\begin{bmatrix} 0 \\ l \\ 0 \end{bmatrix} - \begin{bmatrix} 0 \\ 0 \\ l_p \end{bmatrix}\right) \times \mathbf{F}_{pL}^{te} \\ &= \begin{bmatrix} 0 \\ l \\ 0 \end{bmatrix} \times \left(\mathbf{F}_{pR}^{te} - \mathbf{F}_{pL}^{te}\right) - \begin{bmatrix} 0 \\ 0 \\ l_p \end{bmatrix} \times \left(\mathbf{F}_{pR}^{te} + \mathbf{F}_{pL}^{te}\right) \\ &= \begin{bmatrix} 0 \\ l \\ 0 \end{bmatrix} \times \left(\mathbf{F}_{pR}^{te} - \mathbf{F}_{pL}^{te}\right) - \begin{bmatrix} 0 \\ 0 \\ l_p \end{bmatrix} \times \mathbf{F}_p^{te} \end{aligned} \quad (6)$$

The constraints of the tension will be analyzed later.

C. MOTION EQUATIONS OF THE PARAFOIL

As mentioned above, the parafoil is a kind of flexible wing. However, for the sake of simplicity, the parafoil is assumed to have a fixed structure in shape.

The forces acting on the parafoil are gravity $\mathbf{F}_c^G$, aerodynamic force $\mathbf{F}_c^a$ and tension of suspension lines $\mathbf{F}_c^{te}$ which are represented in Σ_c. Using the Lagrange approach, the basic equations of motion for the parafoil in Σ_c are

$$\begin{aligned} &\frac{\partial \mathbf{P}_c}{\partial t} + \omega_c \times \mathbf{P}_c = \mathbf{F}_c^a + \mathbf{F}_c^G + \mathbf{F}_c^{te} \\ &\frac{\partial \mathbf{H}_c}{\partial t} + \mathbf{V}_c \times \mathbf{P}_c + \omega_c \times \mathbf{H}_c = \mathbf{M}_c^a + \mathbf{M}_c^{te} \end{aligned} \quad (7)$$

where $\mathbf{V}_c = \begin{bmatrix} u_c\ v_c\ w_c \end{bmatrix}^T$ and $\omega_c = \begin{bmatrix} p_c\ q_c\ r_c \end{bmatrix}^T$ are the velocity and angular rate of the parafoil, respectively. The subscript c is the parafoil-fixed coordinate system Σ_c. For the light weighted aircraft with its geometric density close to the air, the apparent mass should be included in calculating the moment and the momentum of moment. Therefore, the following equation holds

$$\begin{bmatrix} \mathbf{P}_c \\ \mathbf{H}_c \end{bmatrix} = [A_a + A_r] \begin{bmatrix} \mathbf{V}_c \\ \omega_c \end{bmatrix} \quad (8)$$

where A_a and A_r are the inertia matrix of the apparent mass and real mass, respectively. A_r is determined by the mass and geometric shape of the parafoil as

$$A_r = \begin{bmatrix} m_c I_3 & 0_{3\times3} \\ 0_{3\times3} & J_c \end{bmatrix} \tag{9}$$

where I_3, $0_{3\times3}$ and J_c are the third-order identity matrix, zero matrix and moment of inertia, respectively. Let b, $\bar{c}$ and t represent the spanwise, mean chord and thickness of the parafoil, respectively. Then, J_c can be simply defined as

$$J_c \approx \begin{bmatrix} b^2+t^2 & 0 & 0 \\ 0 & c^2+t^2 & 0 \\ 0 & 0 & b^2+c^2 \end{bmatrix} \tag{10}$$

The detailed calculation of inertial matrix A_a refers to [7].

To facilitate the derivation, Eq. (8) can be depicted in the form of

$$\begin{bmatrix} \mathbf{P_c} \\ \mathbf{H_c} \end{bmatrix} = \begin{bmatrix} A_1 & A_2 \\ A_3 & A_4 \end{bmatrix} \begin{bmatrix} \mathbf{V}_c \\ \omega_c \end{bmatrix} \tag{11}$$

where $A_i\,(i = 1, 2, 3, 4)$ is the third-order submatrix of $[A_a + A_r]$.

Let $T_{I-c}\left(\zeta_c\ \theta_c\ \psi_c\right)$ be the transformation matrix from Σ_I to Σ_c, then the gravity is expressed as $\mathbf{F}_c^G = T_{I-c}^T\left[0\ 0\ m_c g\right]^T$, where m_c is the mass of the parafoil. The aerodynamic force of the parafoil is composed of aerodynamic lift and aerodynamic drag, and the auxiliary coordinates are utilized to calculate the aerodynamic force. Let $T_{c-r}\left(0\ \mu\ 0\right)$ and $T_{w-r}\left(\beta\ \pi-\alpha\ 0\right)$ be the transformation matrix from Σ_c to Σ_r and Σ_w to Σ_r, respectively. In T_{w-r}, α and β are the angle of attack and sliding angle, which are defined as

$$\begin{cases} \alpha = \tan^{-1}\left(\dfrac{u_a}{w_a}\right) \\ \beta = \tan^{-1}\left(\dfrac{v_a}{|\mathbf{V}_a|^2}\right) \end{cases}$$

where $\mathbf{V}_a = \left[u_a\ v_a\ w_a\right]^T = T_{c-r}\left(\mathbf{V}_c + \mathbf{V}_w\right)$ is the airspeed of the parafoil and $\mathbf{V}_w$ is the external wind disturbance. Then, the aerodynamic force is given as

$$\mathbf{F}_c^a = T_{c-r}^T T_{w-r} Q S_c \begin{bmatrix} C_{D0} + C_{D\alpha^2}\alpha^2 + C_{D\delta_s}\delta_s \\ C_{Y\beta}\beta \\ C_{L0} + C_{L\alpha}\alpha + C_{L\delta_s}\delta_s \end{bmatrix} \tag{12}$$

where C_{D0}, $C_{D\alpha^2}$ and $C_{D\delta_s}$ are the drag coefficients, C_{L0}, $C_{L\alpha}$ and $C_{L\delta_s}$ are the lift coefficients, $C_{Y\beta}$ is the side - force coefficients, S_c is the characteristic area of the parafoil, and $Q = 0.5\rho|\mathbf{V}_a|^2$ represents the dynamic pressure, respectively. δ_s is the symmetric deflection and is defined as $\delta_s = \min\{\delta_R, \delta_L\}$ [25], where δ_R and δ_L are the deflection control of the right and left trailing edge, respectively. With the aerodynamic derivative coefficients $C_{l\beta}$, C_{lp} etc., the aerodynamic moment $\mathbf{M}_c^a$ is defined as

$$\begin{aligned} \mathbf{M}_c^a &= T_{c-r}^T T_{w-r} Q S_c \\ &\times \begin{bmatrix} b\left(C_{l\beta}\beta + \dfrac{b}{2|\mathbf{V}_a|}\left(C_{lp}p_c + C_{lr}r_c\right) + C_{l\delta_a}\delta_a\right) \\ \bar{c}\left(C_{m0} + C_{m\alpha}\alpha + \dfrac{\bar{c}}{2|\mathbf{V}_a|}C_{mq}q\right) \\ b\left(C_{n\beta}\beta + \dfrac{b}{2|\mathbf{V}_a|}\left(C_{np}p + C_{nr}r\right) + C_{n\delta_a}\delta_a\right) \end{bmatrix} \end{aligned} \tag{13}$$

where $\delta_a = \delta_L - \delta_R$ is the asymmetric deflection.

In Σ_c, $\mathbf{F}_c^{te}$ is defined as $\mathbf{F}_c^{te} = \mathbf{F}_{cR}^{te} + \mathbf{F}_{cL}^{te}$ with $\mathbf{F}_{cR}^{te}$ and $\mathbf{F}_{cL}^{te}$ are the tensions acting on C_R and C_L, respectively. Let l_c be the distance from C_m to O_c, the moment produced by suspension lines is given as

$$\mathbf{M}_c^{te} = \mathbf{L}_{cR} \times \mathbf{F}_{cR}^{te} + \mathbf{L}_{cL} \times \mathbf{F}_{cL}^{te} \tag{14}$$

where

$$\begin{aligned} \mathbf{L}_{cR} &= T_{c-p}^T \begin{bmatrix} 0 \\ l \\ 0 \end{bmatrix} + \begin{bmatrix} 0 \\ 0 \\ l_c \end{bmatrix}, \\ \mathbf{L}_{cL} &= T_{c-p}^T \begin{bmatrix} 0 \\ -l \\ 0 \end{bmatrix} + \begin{bmatrix} 0 \\ 0 \\ l_c \end{bmatrix} \end{aligned} \tag{15}$$

are the position of C_R and C_L in Σ_c, respectively. Substituting Eq. (15) into Eq. (14), we obtain

$$\begin{aligned} \mathbf{M}_c^{te} &= \left(T_{c-p}^T \begin{bmatrix} 0 \\ l \\ 0 \end{bmatrix} + \begin{bmatrix} 0 \\ 0 \\ l_c \end{bmatrix}\right) \times \mathbf{F}_{cR}^{te} \\ &+ \left(-T_{c-p}^T \begin{bmatrix} 0 \\ l \\ 0 \end{bmatrix} + \begin{bmatrix} 0 \\ 0 \\ l_c \end{bmatrix}\right) \times \mathbf{F}_{cL}^{te} \\ &= T_{c-p}^T \begin{bmatrix} 0 \\ l \\ 0 \end{bmatrix} \times \left(\mathbf{F}_{cR}^{te} - \mathbf{F}_{cL}^{te}\right) + \begin{bmatrix} 0 \\ 0 \\ l_c \end{bmatrix} \times \left(\mathbf{F}_{cR}^{te} + \mathbf{F}_{cL}^{te}\right) \\ &= T_{c-p}^T \left(\begin{bmatrix} 0 \\ l \\ 0 \end{bmatrix} \times \left(T_{c-p}\left(\mathbf{F}_{cR}^{te} - \mathbf{F}_{cL}^{te}\right)\right)\right) + \begin{bmatrix} 0 \\ 0 \\ l_c \end{bmatrix} \times \mathbf{F}_c^{te} \end{aligned} \tag{16}$$

III. CONSTRAINT ANALYSIS AND DYNAMIC MODELING OF THE PPF

Eq. (2) and (7) give the basic motion equations of the PPF, and it is sufficient to establish a six DOF dynamic model of the PPF without considering the relative motion between the payload and parafoil. However in eight DOF dynamic model, the constraints, including velocity constraint, angular rate constraint and force constraint should be considered and dealt with.

A. VELOCITY CONSTRAINT

The payload has the relative pitch and yaw motions to the parafoil. According to Fig. 2, the middle point C_m of suspending points C_R and C_L is fixed to both Σ_c and Σ_p, and the velocity of C_m can be defined respectively as

$$\begin{cases} \mathbf{V}_{cc} = \mathbf{V}_c + \omega_c \times \mathbf{L}_{cc} \\ \mathbf{V}_{pc} = \mathbf{V}_p + \omega_p \times \mathbf{L}_{pc} \end{cases} \tag{17}$$

where $\mathbf{L}_{cc} = \begin{bmatrix} 0 & 0 & l_c \end{bmatrix}$ and $\mathbf{L}_{pc} = \begin{bmatrix} 0 & 0 & -l_p \end{bmatrix}$ are the positions of C_m in Σ_c and Σ_p, respectively.If we redefine $\mathbf{V}_{cc}$ and $\mathbf{V}_{pc}$ in Σ_I, Eq. (17) can then be rewritten as

$$T_{I-c}^T (\mathbf{V}_c + \omega_c \times \mathbf{L}_{cc}) = T_{I-p}^T \left(\mathbf{V}_p + \omega_p \times \mathbf{L}_{pc}\right) \tag{18}$$

Differentiating Eq. (18) gives

$$\begin{aligned} &T_{I-c}^T (\omega_c \times (\mathbf{V}_c + \omega_c \times \mathbf{L}_{cc})) + T_{I-c}^T \left(\dot{\mathbf{V}}_c + \dot{\omega}_c \times \mathbf{L}_{cc}\right) \\ &= T_{I-p}^T \left(\omega_p \times \left(\mathbf{V}_p + \omega_p \times \mathbf{L}_{pc}\right)\right) + T_{I-p}^T \left(\dot{\mathbf{V}}_p + \dot{\omega}_p \times \mathbf{L}_{pc}\right) \end{aligned} \tag{19}$$

which can be reformulated as

$$\begin{aligned} &\dot{\mathbf{V}}_c + \dot{\omega}_c \times \mathbf{L}_{cc} - T_{c-p}^T \left(\dot{\mathbf{V}}_p + \dot{\omega}_p \times \mathbf{L}_{pc}\right) \\ &= -\omega_c \times (\mathbf{V}_c + \omega_c \times \mathbf{L}_{cc}) + T_{c-p}^T \left(\omega_p \times \left(\mathbf{V}_p + \omega_p \times \mathbf{L}_{pc}\right)\right) \end{aligned} \tag{20}$$

This gives three equations of the velocity constraint.

B. ANGULAR RATE CONSTRAINT

According to the principles of theoretical mechanics, the angular rate constraint of the PPF is given as

$$\begin{bmatrix} p_p \\ q_p \\ r_p \end{bmatrix} - T_{c-p} \begin{bmatrix} p_c \\ q_c \\ r_c \end{bmatrix} = \begin{bmatrix} 0 & 0 & -\sin(\theta_r) \\ 0 & 1 & 0 \\ 0 & 0 & \cos(\theta_r) \end{bmatrix} \begin{bmatrix} 0 \\ \dot{\theta}_r \\ \dot{\psi}_r \end{bmatrix} \tag{21}$$

where θ_r and ψ_r are relative pitch angle and relative yaw angle, respectively. To facilitate the constraint analysis, Eq. (21) can be reformulated as

$$\begin{aligned} &\begin{bmatrix} 0 \\ q_p \\ r_p \end{bmatrix} - T_{c-p} \begin{bmatrix} p_c \\ q_c \\ r_c \end{bmatrix} \\ &= \begin{bmatrix} -1 & 0 & -\sin(\theta_r) \\ 0 & 1 & 0 \\ 0 & 0 & \cos(\theta_r) \end{bmatrix} \begin{bmatrix} 0 \\ \dot{\theta}_r \\ \dot{\psi}_r \end{bmatrix} + \begin{bmatrix} -1 & 0 & -\sin(\theta_r) \\ 0 & 1 & 0 \\ 0 & 0 & \cos(\theta_r) \end{bmatrix} \begin{bmatrix} p_p \\ 0 \\ 0 \end{bmatrix} \\ &= \begin{bmatrix} -1 & 0 & -\sin(\theta_r) \\ 0 & 1 & 0 \\ 0 & 0 & \cos(\theta_r) \end{bmatrix} \begin{bmatrix} p_p \\ \dot{\theta}_r \\ \dot{\psi}_r \end{bmatrix} \end{aligned} \tag{22}$$

which is equivalent to

$$\begin{aligned} &\begin{bmatrix} p_p \\ \dot{\theta}_r \\ \dot{\psi}_r \end{bmatrix} \\ &= \begin{bmatrix} 0 & 0 & -\sin(\theta_r) \\ 0 & 1 & 0 \\ 0 & 0 & \cos(\theta_r) \end{bmatrix}^{-1} \left(\begin{bmatrix} 0 \\ q_p \\ r_p \end{bmatrix} - T_{c-p} \begin{bmatrix} p_c \\ q_c \\ r_c \end{bmatrix} \right) \\ &= \begin{bmatrix} -1 & 0 & -\tan(\theta_r) \\ 0 & 1 & 0 \\ 0 & 0 & 1/\cos(\theta_r) \end{bmatrix} \left(\begin{bmatrix} 0 \\ q_p \\ r_p \end{bmatrix} - T_{c-p} \begin{bmatrix} p_c \\ q_c \\ r_c \end{bmatrix} \right) \end{aligned} \tag{23}$$

The first row of Eq. (23) can be rewritten as

$$\begin{aligned} p_p &= -\tan(\theta_r) r_p + \frac{\cos(\psi_r)}{\cos(\theta_r)} p_c + \frac{\sin(\psi_r)}{\cos(\theta_r)} q_c \\ &\Rightarrow \cos(\theta_r) p_p = -\sin(\theta_r) r_p + \cos(\psi_r) p_c + \sin(\psi_r) q_c \end{aligned} \tag{24}$$

Differentiating Eq. (24) we obtain

$$\begin{aligned} &-\dot{\theta}_r \sin(\theta_r) p_p + \cos(\theta_r) \dot{p}_p \\ &= -\dot{\theta}_r \cos(\theta_r) r_p - \sin(\theta_r) \dot{r}_p - \dot{\psi}_r \sin(\psi_r) p_c \\ &\quad + \cos(\psi_r) \dot{p}_c + \dot{\psi}_r \cos(\psi_r) q_c + \sin(\psi_r) \dot{q}_c \end{aligned} \tag{25}$$

which also is

$$\mathbf{K_1} \dot{\omega}_p - \mathbf{K_2} \dot{\omega}_c = \mathbf{K_3} \omega_p + \mathbf{K_4} \omega_c \tag{26}$$

where

$$\begin{cases} \mathbf{K}_1 = \begin{bmatrix} \cos(\theta_r) & 0 & \sin(\theta_r) \end{bmatrix} \\ \mathbf{K}_2 = \begin{bmatrix} \cos(\psi_r) & \sin(\psi_r) & 0 \end{bmatrix} \\ \mathbf{K}_3 = \begin{bmatrix} \dot{\theta}_r \sin(\theta_r) & 0 & -\dot{\theta}_r \cos(\theta_r) \end{bmatrix} \\ \mathbf{K}_4 = \begin{bmatrix} -\dot{\psi}_r \sin(\psi_r) & \dot{\psi}_r \cos(\psi_r) & 0 \end{bmatrix} \end{cases}$$

This gives the angular rate constraint.

C. FORCE CONSTRAINT

According to Newton's third law, the forces acting on the suspending points C_R and C_L are described as

$$\begin{aligned} &\mathbf{F}_{cR}^{te} = -T_{c-p}^T \mathbf{F}_{pR}^{te}, \mathbf{F}_{cL}^{te} = -T_{c-p}^T \mathbf{F}_{pL}^{te} \\ &\Rightarrow \mathbf{F}_c^{te} = -T_{c-p}^T \mathbf{F}_p^{te} \end{aligned} \tag{27}$$

Therefore, the effect of the difference between tensions expressed in Eq. (6) and Eq. (16) can be reformulated as

$$\begin{aligned} &\begin{bmatrix} 0 \\ l \\ 0 \end{bmatrix} \times \left(\mathbf{F}_{pR}^{te} - \mathbf{F}_{pL}^{te}\right) \\ &= \begin{bmatrix} 0 & 0 & l \\ 0 & 0 & 0 \\ -l & 0 & 0 \end{bmatrix} \left(\mathbf{F}_{pR}^{te} - \mathbf{F}_{pL}^{te}\right) \\ &= \begin{bmatrix} 1 & 0 \\ 0 & 0 \\ 0 & 1 \end{bmatrix} \begin{bmatrix} m_x^{te} \\ m_z^{te} \end{bmatrix} \\ &= \begin{bmatrix} \mathbf{E}_1 & \mathbf{E}_2 \end{bmatrix} \begin{bmatrix} m_x^{te} \\ m_z^{te} \end{bmatrix} \end{aligned} \tag{28}$$

$$\begin{aligned} &\begin{bmatrix} 0 \\ l \\ 0 \end{bmatrix} \times \left(T_{c-p} \left(\mathbf{F}_{cR}^{te} - \mathbf{F}_{cL}^{te}\right)\right) \\ &= -\begin{bmatrix} 0 & 0 & l \\ 0 & 0 & 0 \\ -l & 0 & 0 \end{bmatrix} \left(\mathbf{F}_{pR}^{te} - \mathbf{F}_{pL}^{te}\right) \end{aligned}$$

$$
\begin{aligned}
&= -\begin{bmatrix} 1 & 0 \\ 0 & 0 \\ 0 & 1 \end{bmatrix} \begin{bmatrix} m_x^{te} \\ m_z^{te} \end{bmatrix} \\
&= -\begin{bmatrix} \mathbf{E}_1 & \mathbf{E}_2 \end{bmatrix} \begin{bmatrix} m_x^{te} \\ m_z^{te} \end{bmatrix}
\end{aligned}
\tag{29}
$$

where $\mathbf{E}_1 = \begin{bmatrix} 1 & 0 & 0 \end{bmatrix}^T$ and $\mathbf{E}_2 = \begin{bmatrix} 0 & 0 & 1 \end{bmatrix}^T$. m_x^{te} and m_z^{te} are the first and third terms of the moment $\mathbf{M}_{pd}^{te}$ produced by $\left(\mathbf{F}_{pR}^{te} - \mathbf{F}_{pL}^{te}\right)$ and $\mathbf{M}_{pd}^{te}$ is defined as

$$
\mathbf{M}_{pd}^{te} = \begin{bmatrix} 0 \\ l \\ 0 \end{bmatrix} \times \left(\mathbf{F}_{pR}^{te} - \mathbf{F}_{pL}^{te}\right) \tag{30}
$$

The configuration of the PPF allows relative yawing motion about the z_c-axis, and the moment due to the tensions is given in Eq. (16). We assume that m_{cz}^{te}, which is the third term of $\mathbf{M}_c^{te}$, is proportional to ψ_r, $\dot{\psi}_r$, and the third component of $\mathbf{F}_c^{te}$. Then, m_{cz}^{te} can be described as

$$
\begin{aligned}
m_{cz}^{te} &= \begin{bmatrix} 0 & 0 & 1 \end{bmatrix} \mathbf{M}_c^{te} \\
&= \mathbf{E}_2^T \left(-T_{c-p}^T \left(\begin{bmatrix} \mathbf{E}_1 & \mathbf{E}_2 \end{bmatrix} \begin{bmatrix} m_x^{te} \\ m_z^{te} \end{bmatrix} \right) + \begin{bmatrix} 0 \\ 0 \\ l_c \end{bmatrix} \times \mathbf{F}_c^{te} \right) \\
&= -\left(kF_{cz}^{te}\psi_r + c\dot{\psi}_r\right)
\end{aligned}
\tag{31}
$$

where k and c are positive constants, and F_{cz}^{te} is the z_c-axis component of $\mathbf{F}_c^{te}$. Eq. (31) can be rewritten as

$$
\begin{aligned}
&\mathbf{E}_2^T \left(S\left(l_c\mathbf{E}_2\right) - k\psi_r\right) T_{c-p}^T \mathbf{F}_p^{te} \\
&\quad + \mathbf{E}_2^T T_{c-p}^T \begin{bmatrix} \mathbf{E}_1 & \mathbf{E}_2 \end{bmatrix} \begin{bmatrix} m_x^{te} \\ m_z^{te} \end{bmatrix} T_{c-p}^T \mathbf{F}_p^{te} = c\dot{\psi}_r
\end{aligned}
\tag{32}
$$

where $S(\cdot) : \mathbb{R}^3 \rightarrow so(3)$ transforms a vector into a skew-symmetric matrix, such that $\mathbf{x} \times \mathbf{y} = S(x)\, y$ for any $\mathbf{x}, \mathbf{y} \in \mathbb{R}^3$. This gives one equation of the force constraint.

D. DYNAMIC MODEL OF THE PPF

Substituting Eq. (3) and Eq. (11) into Eq. (2) and Eq. (7), respectively. Then we obtain

$$
A_p\dot{\mathbf{V}}_p + \omega_p \times A_p\mathbf{V}_p = \mathbf{F}_p^a + \mathbf{F}_p^G + \mathbf{F}_p^{th} + \mathbf{F}_p^{te} \tag{33}
$$

$$
J_p\dot{\omega}_p + \omega_p \times J_p\omega_p = \begin{bmatrix} \mathbf{E}_1 & \mathbf{E}_2 \end{bmatrix} \begin{bmatrix} m_x^{te} \\ m_z^{te} \end{bmatrix} - l_p S\left(\mathbf{E}_2^T\right) \mathbf{F}_p^{te} \tag{34}
$$

$$
A_1\dot{\mathbf{V}}_c + A_2\dot{\omega}_c + \omega_c \times \left(A_1\mathbf{V}_c + A_2\omega_c\right) = \mathbf{F}_c^a + \mathbf{F}_c^G + \mathbf{F}_c^{te} \tag{35}
$$

$$
\begin{aligned}
&A_3\dot{\mathbf{V}}_c + A_4\dot{\omega}_c + \mathbf{V}_c \times \left(A_1\mathbf{V}_c + A_2\omega_c\right) \\
&\quad + \omega_c \times \left(A_3\mathbf{V}_c + A_4\omega_c\right) \\
&= M_c^a - T_{c-p}^T \left(\begin{bmatrix} \mathbf{E}_1 & \mathbf{E}_2 \end{bmatrix} \begin{bmatrix} m_x^{te} \\ m_z^{te} \end{bmatrix} \right) + l_c S\left(\mathbf{E}_2^T\right) \mathbf{F}_c^{te}
\end{aligned}
\tag{36}
$$

Let $\dot{x} = \begin{bmatrix} \dot{\mathbf{V}}_p & \dot{\omega}_p & \dot{\mathbf{V}}_c & \dot{\omega}_c & \mathbf{F}_c^{te} & m_x^{te} & m_z^{te} \end{bmatrix}^T$ be the time derivative of the states, then we have 17 equations with Eq. (33), (34), (35), (36), (20), (25) and (31) to calculate the states.

In summary, the motion of equations of the PPF can be described as

$$
\dot{x} = M^{-1}F \tag{37}
$$

where M and F are defined in Eq. (38) and Eq. (39), as shown at the bottom of this page.

The eight DOF dynamic model of the PPF is obtained by applying the constraints of Eq. (19) and (21). The auxiliary states, $\mathbf{F}_c^{te}$, m_x^{te} and m_z^{te}, which are useful in mechanical analysis, are calculated at the same time.

IV. NUMERICAL SIMULATION AND ANALYSIS

The dynamic model of the PPF is established for numerical simulation of the practical equipment. The basic motion characteristics, including translational and rotational motions, can be primarily investigated through numerical simulation. The characteristic parameters of the concerned PPF and the aerodynamic parameters of the parafoil are listed in Table 1 and Table 2.

$$
M = \begin{bmatrix}
A_p & 0_{3\times3} & 0_{3\times3} & 0_{3\times3} & -I_3 & 0_{3\times1} & 0_{3\times1} \\
0_{3\times3} & J_p & 0_{3\times3} & 0_{3\times3} & S\left(l_p\mathbf{E}_1\right) & -\mathbf{E}_2 & -\mathbf{E}_1 \\
0_{3\times3} & 0_{3\times3} & A_1 & A_2 & T_{c-p}^T & 0_{3\times1} & 0_{3\times1} \\
0_{3\times3} & 0_{3\times3} & A_3 & A_4 & S\left(l_c\mathbf{E}_1\right) T_{c-p}^T & T_{c-p}^T\mathbf{E}_2 & T_{c-p}^T\mathbf{E}_1 \\
-T_{c-p}^T & T_{c-p}^T S\left(\mathbf{L}_{pc}\right) & I_3 & -S\left(\mathbf{L}_{cc}\right) & 0_{3\times3} & 0_{3\times1} & 0_{3\times1} \\
0_{1\times3} & \mathbf{K}_1 & 0_{1\times3} & \mathbf{K}_2 & 0_{1\times3} & 0 & 0 \\
0_{1\times3} & 0_{1\times3} & 0_{1\times3} & 0_{1\times3} & -\mathbf{E}_1^T \left(S\left(l_c\mathbf{E}_1\right) - k\psi_r\right) T_{c-p}^T & -\mathbf{E}_1^T T_{c-p}^T \mathbf{E}_2 & -\mathbf{E}_1^T T_{c-p}^T \mathbf{E}_1
\end{bmatrix}
\tag{38}
$$

$$
F = \begin{bmatrix}
-S\left(\omega_p\right) A_p\mathbf{V}_p + \mathbf{F}_p^a + \mathbf{F}_p^G + \mathbf{F}_p^{th} \\
-S\left(\omega_p\right) J_p\omega_p \\
-S\left(\omega_c\right)\left(A_1\mathbf{V}_c + A_2\omega_c\right) + \mathbf{F}_c^a + \mathbf{F}_c^G \\
-S\left(\mathbf{V}_c\right)\left(A_1\mathbf{V}_c + A_2\omega_c\right) - S\left(\omega_c\right)\left(A_3\mathbf{V}_c + A_4\omega_c\right) + \mathbf{M}_c^a \\
-S\left(\omega_c\right)\left(\mathbf{V}_c + S\left(\omega_c\right)\mathbf{L}_{cc}\right) + T_{c-p}^T S\left(\omega_p\right)\left(\mathbf{V}_p + S\left(\omega_p\right)\mathbf{L}_{pc}\right) \\
K_3\omega_p + K_4\omega_c \\
c\dot{\psi}_r
\end{bmatrix}
\tag{39}
$$

TABLE 1. Characteristic parameters of the PPF.

Symbol	Description	Value
b	Wing span	$11.18/m$
$\bar{c}$	Mean aerodynamic chord	$2.23/m$
t	Thickness	$0.34/m$
μ	Rigging angle	-7/°
S_c	Wing area	$24.97/m^2$
l_c	O_c to O_m	$6.28/m$
l_p	O_m to O_p	$0.5/m$
l	O_m to $O_R(O_L)$	$0.25/m$
m_c	Mass of parafoil	$6.9/kg$
m_p	Mass of payload	$76.5/kg$
S_p	Payload area	$0.6/m^2$

TABLE 2. Aerodynamic parameters of the parafoil.

Symbol	Value	Symbol	Value
C_{D0}	0.13	$C_{D\alpha}$	1.11
$C_{D\delta_s}$	0.58	$C_{Y\beta}$	-0.46
C_{L0}	0.50	$C_{L\alpha}$	3.51
$C_{L\delta_s}$	0	$C_{L\beta}$	0
C_{lp}	0.42	C_{lr}	0.00
$C_{l\delta_a}$	0.002	C_{m0}	0.19
$C_{m\alpha}$	-0.04	C_{mq}	-2.00
$C_{n\beta}$	0.00	C_{np}	0.00
C_{nr}	-0.14	$C_{n\delta_a}$	-0.02

A. STEADY FLIGHT

The PPF will operate in a steady state without manipulation. In this section, the initial velocity condition is set as $\mathbf{V}_c = \mathbf{V}_p = \begin{bmatrix} 8.3 & 0 & 1.2 \end{bmatrix}$ m/s and the Euler angles are set to be zero. Fig. 3 and Fig. 4 show the time responses of the velocity and attitude of the PPF. From Fig. 3, it can be seen that v_y maintains 0 m/s since there is no turning manipulation. Combining Fig. 3 and Fig. 4, we see that the horizontal and vertical velocities along x_I and z_I-axis converge to the specific value, respectively. And the Euler angles also obtain steady states after oscillations. After a period of regulation, the velocity of the PPF along x_I and z_I axis, v_x and v_z, maintain at 8.23 m/s and 1.27 m/s, respectively. Fig. 4 illustrates that the Euler angles and the relative rotation angles. The pitch angle θ_c oscillates in 50 s and then maintains the value of 5° until the end, while the relative pitch angle θ_r maintains -4.69° after 31 s.

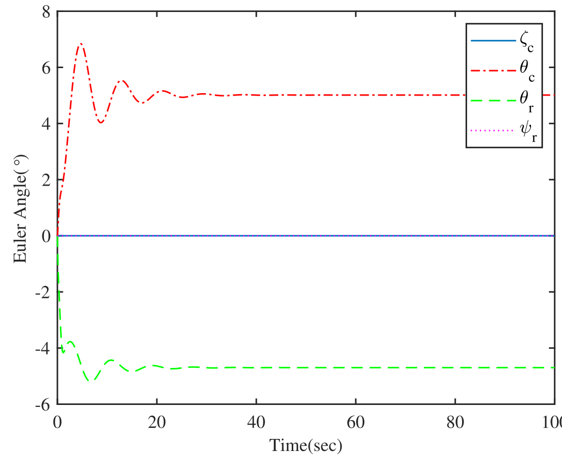

FIGURE 4. Euler angles of steady flight.

B. DEFLECTION CONTROL

The flight direction of the PPF is regulated by the deflection of trailing edge. The left trailing edge is pulled down steadily and δ_L is set as 30% at 20 s. Therefore, the PPF turns left due to the deflection control. The corresponding motion characteristics are shown in Fig. 5 - Fig. 7. Fig. 5 indicates the velocity in Σ_I. The horizontal trajectory of the PPF is a circle. Therefore, the velocities along x_I and y_I after 20 s is sine-wave shaped. Actually, the magnitude of the horizontal velocity remains the same with steady flight without wind disturbance. The Euler angles of the PPF are shown in Fig. 6. According to Fig. 6, the final values of θ_c and ψ_r are the same with those of the steady flight, respectively. ζ_c maintains 3.18° and ψ_r converges to zero after oscillation. The responses of different δ_L of 30%, 50% and 80% are shown in Fig. 7. The radii of the circular trajectories are 254.5 m,

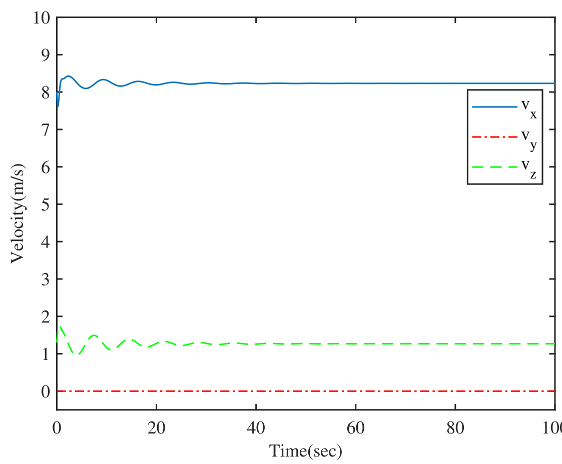

FIGURE 3. Velocity of steady flight.

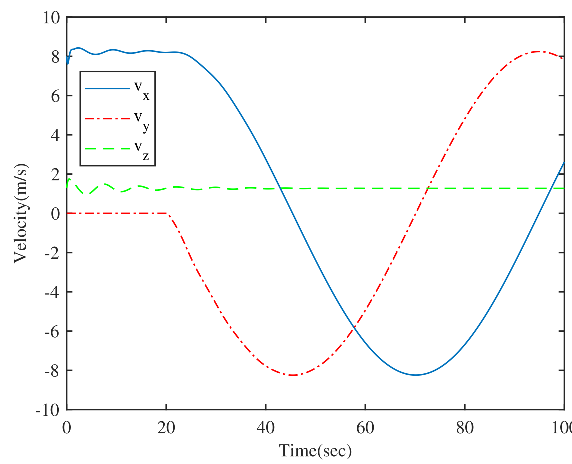

FIGURE 5. Velocity of deflection control (Left, 30%).

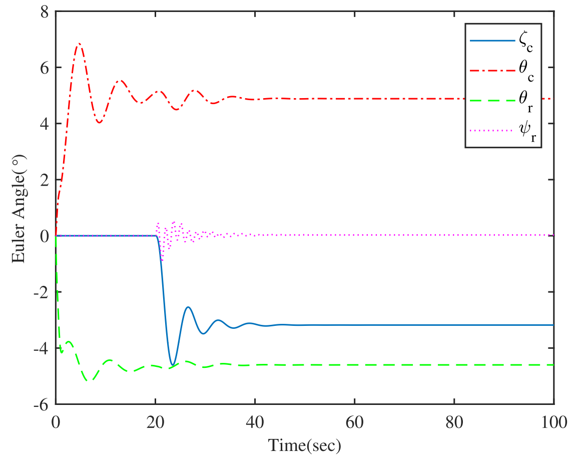

FIGURE 6. Euler angles of deflection control (Left, 30%).

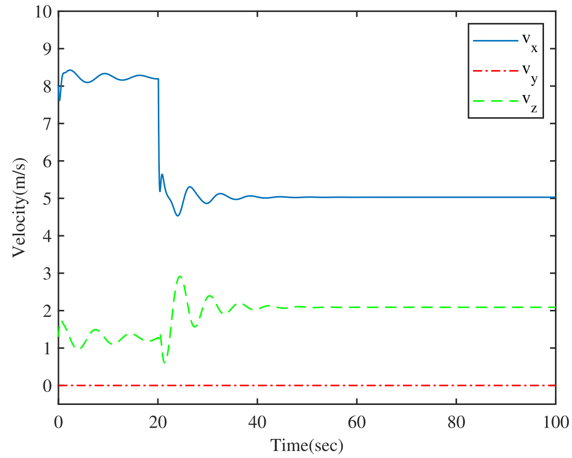

FIGURE 8. Velocity of flare-landing.

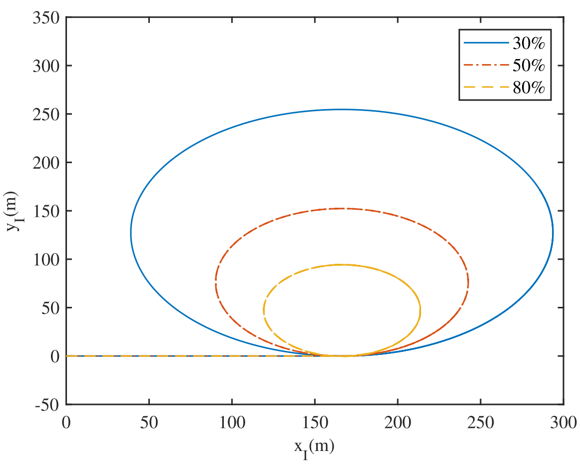

FIGURE 7. Turning response of different deflection control.

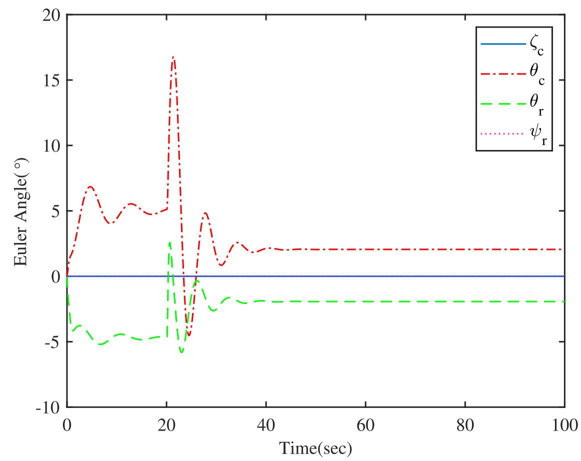

FIGURE 9. Euler angles of flare-landing.

152.3 m and 94.3 m, respectively. Fig. 7 shows that $\dot{\psi}_c$ and δ_L are positively correlated.

In the control of the PPF, the asymmetric deflection of δ_R and δ_L correspond to the turning and direction manipulation, while the symmetric deflection control of δ_R and δ_L mainly control the longitudinal dynamics. This characteristic provides the parafoil-based aero vehicles the flare-landing capability, also called soft-landing. Fig. 8 - Fig. 9 show the velocity and attitude response of flare-landing control with δ_R and δ_L reaching their maxima at 20 s. As shown in Fig. 8, the horizontal velocity maintains 4.54 m/s after 4.02 s of flare-landing control, and then maintains 5.03 m/s after 21.5 s. The vertical velocity increases to 2.08 m/s at 23 s after a short time of decrease. If we pull down the trailing edge to the maximum 1.43 s before landing, then we obtain the landing velocity of 5.23 m/s in horizontal direction and 0.61 m/s in vertical direction, which are much lower than that of steady flight. It means that the PPF can achieve soft-landing with low reluctant velocity which will cause little or even no damage to the equipment. Fig. 9 illustrates the attitudes of flare-landing. The pitch angle increases rapidly from 5° to 16.7° at the beginning and oscillates from 16.7° to -4.5° only within 3.1 s. The steady values of pitch angle and relative pitch angle are both alleviated due to flare-landing.

The coupling between the longitudinal and lateral control is an important factor to be addressed in dynamic analysis. The coupling effect of the deflection on the longitudinal dynamics is shown in Fig. 10. The thrust of 50 N and δ_L of 20%, 40% and 60% are added to simulation at 20 s. It is clear that the deflection has a limited impact on the longitudinal velocity. Therefore, the coupling factor is ignored in the design of longitudinal controller.

C. THRUST CONTROL

The thrust provided by the propeller is another control input for the PPF, which is applied to control longitudinal position. Fig. 11 and Fig. 12 show the velocities and Euler angles of the PPF with thrust input. Fig. 11 shows the velocity response of 50 N thrust. The lateral velocity v_x is almost constant after 24.6 s of vibration. However, the longitudinal velocity decreases from 1.27 m/s to 0.75 m/s, with a transient time of 33.5 s after the thrust is added. According to Fig. 12,

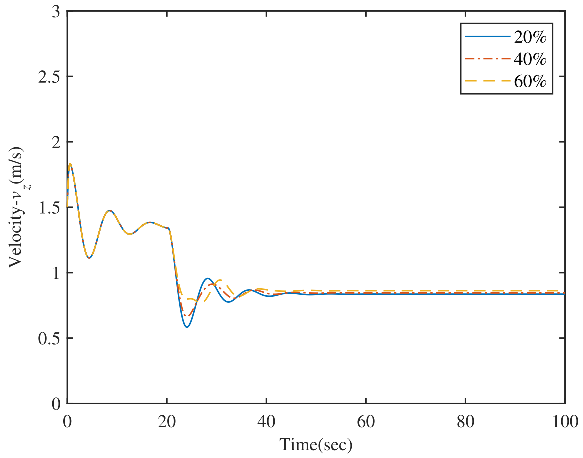

FIGURE 10. Coupling effect of deflection on longitudinal control.

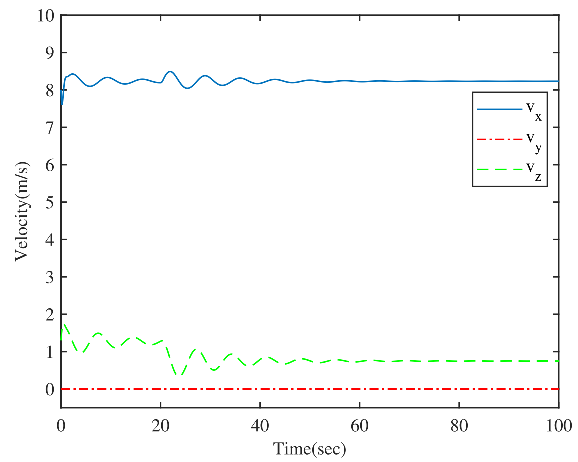

FIGURE 11. Velocity of thrust control.

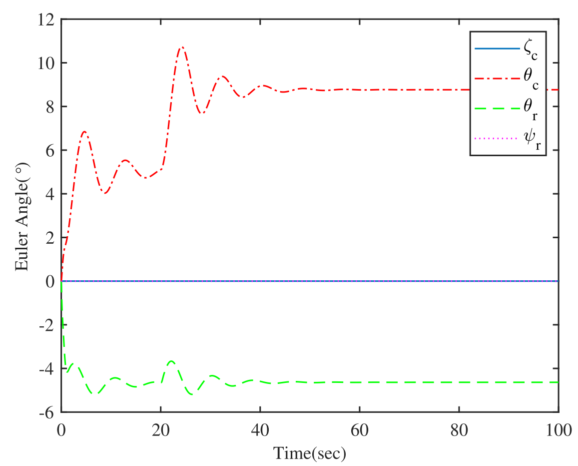

FIGURE 12. Euler angles of thrust control.

the relative pitch angle also stays unchanged compared with Fig. 4, while the pitch angle increases to 8.8°.

The longitudinal motion responses of different thrusts are illustrated in Fig. 13. For the given model, the thrust of 123.2 N can make the PPF fly at a fixed altitude. As shown in Fig. 13, the altitude of the PPF decreases with the thrust of 50 N and 90 N, and increases with the thrust of 130 N.

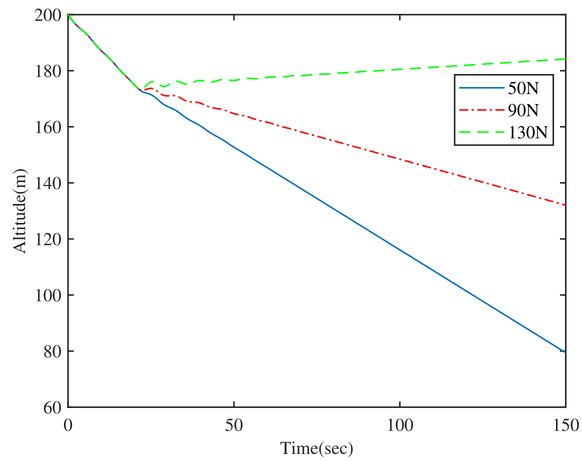

FIGURE 13. Altitude of different thrust control.

Since the thrust input affects the pitch angle, the thrust interacts with the deflection control. The horizontal responses of different thrust inputs with $\delta_L = 30\%$ are shown in Fig. 14. The radii of the horizontal trajectories are 254.6 m, 252.4 m and 243.3 m, corresponding to the thrust of 50 N, 90 N and 130 N. It is concluded that the longitudinal control affects the lateral control

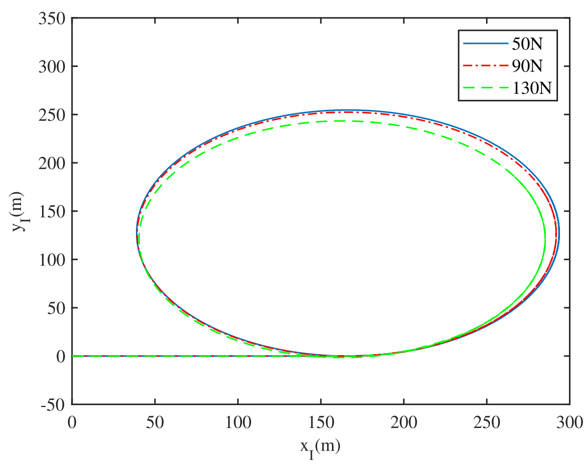

FIGURE 14. Coupling effect of thrust on lateral control.

D. WIND RESPONSE

The mean geometric density of the parafoil is close to the air. As a result, the PPF is sensitive to the wind. In this section, the wind speed is set to be $\mathbf{V}_w = \begin{bmatrix} 3 & -2 & 0 \end{bmatrix} m/s$ and is added to the model at 20 s. And the deflection is set to be 30% on the left. Fig. 15 shows the trajectory of the PPF subject to the wind. It is shown that the trajectory becomes a curve which is in line with the wind direction, instead of a circle. Fig. 16 illustrates the velocity of the PPF. Compared with Fig. 6,

Fig. 17 shows that the pitch angle is substantially affected by the wind.

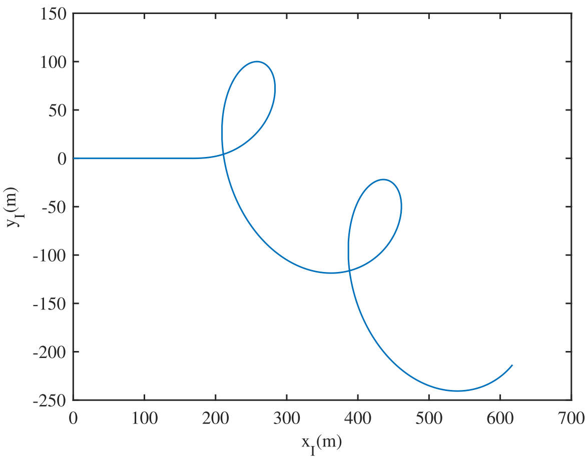

FIGURE 15. Trajectory of the PPF in wind.

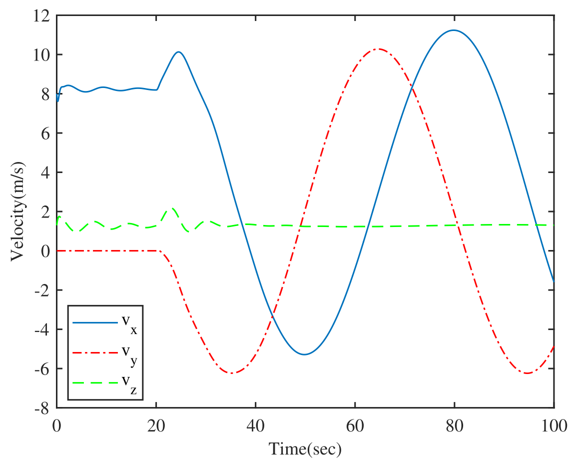

FIGURE 16. Velocity of the PPF in wind.

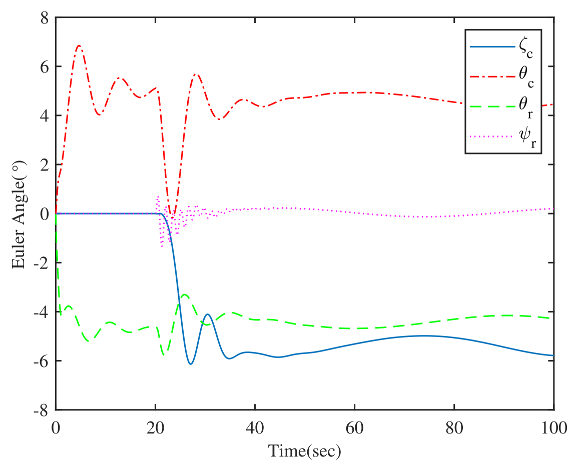

FIGURE 17. Euler angles of the PPF in wind.

V. VALIDATION OF THE PROPOSED MODEL

To evaluate the validity of the dynamic model, the numerical simulations are carried out and the results are compared with the experimental data.

The experimental data of a free flight test, which was implemented for the model validation, is shown in Fig. 18 - Fig. 20. The initial condition of the simulation is set according to the experimental data. As mentioned above, the dynamics of the PPF is very sensitive to the wind. While in reality, the wind speed is time-varying at low altitudes and it is hard to measure. Therefore, the wind is assumed to be constant and the mean wind speed is used in the simulation. Fig. 18 shows the horizontal trajectory of the experimental and the simulated data. The corresponding simulation lasts for 65 *s*. The simulated trajectory is a little different from the practical trajectory. However, the difference is acceptable. Fig. 19 shows the velocities in Σ_I. According to Fig. 19, the calculated velocities are quite close to the corresponding experimental ones with similar low-frequency components. The comparison of Euler angles are shown in Fig. 20. The numerical simulation agrees with that of the experimental data.

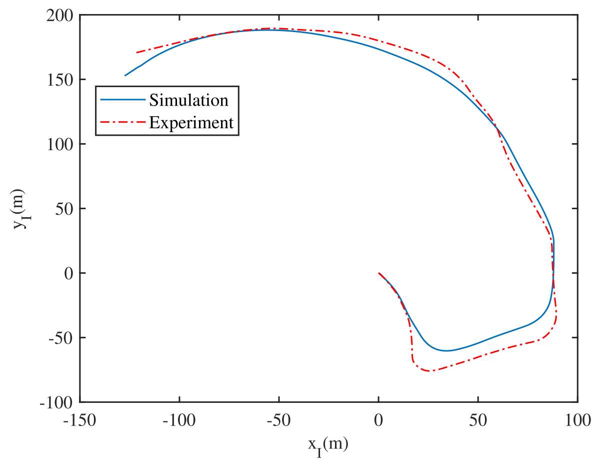

FIGURE 18. Horizontal trajectory of the flight test.

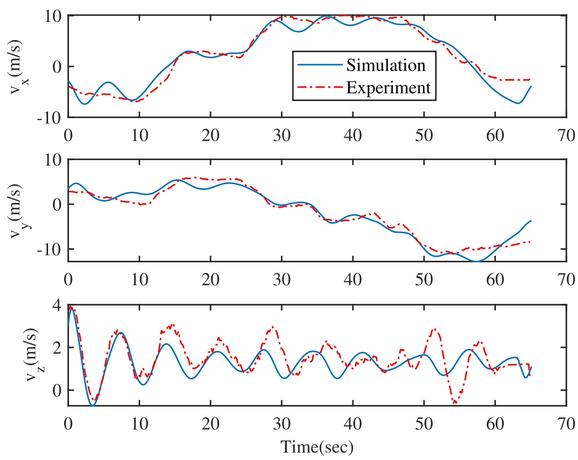

FIGURE 19. Velocity of the flight test.

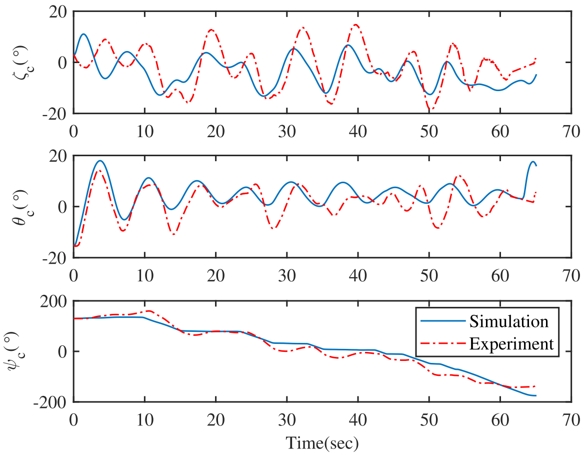

FIGURE 20. **Euler angle of the flight test.**

In summary, the results indicate that the developed model matches the practical dynamics well.

VI. CONCLUSION

To achieve the precise simulation of the PPF, the nonlinear model based on Lagrangian equations and dynamic constraints was proposed. The model was obtained as a state-vector equation by eliminating all the internal forces and the detailed motion equations were derived and presented. The numerical simulations were performed based on the proposed model to investigate the dynamic characteristics and the control ability. The simulation results with deflection in the presence of wind disturbance indicate the unique characteristics of the PPF. Moreover, the lateral and the longitudinal dynamics are coupled in control. In particular, the PPF has the soft-landing capability and the model was implemented to derive the proper altitude for landing control. The numerical simulation results were compared with the experimental data, which indicates that the developed model describes the dynamics of the PPF considerably well. This can provide a solid foundation for further aerodynamic identification and control development.

REFERENCES

[1] S. Lee and A. Arena, "Autonomous parafoil return-to-point vehicle for high altitude ballooning," in *Proc. AIAA Guid., Navigat., Control Conf.*, Jan. 2014, pp. 1–15.

[2] S. Z. Luo, Q. L. Sun, W. N. Wu, M. W. Sun, Z. Q. Chen, and Y. P. He, "Accurate flight path tracking control for powered parafoil aerial vehicle using ADRC-based wind feedforward compensation," *Aerosp. Sci. Technol.*, vol. 84, pp. 904–915, Jan. 2019.

[3] S. Z. Luo, Q. L. Sun, M. W. Sun, P. L. Tan, W. N. Wu, H. Sun, and Z. Q. Chen, "On decoupling trajectory tracking control of unmanned powered parafoil using ADRC-based coupling analysis and dynamic feedforward compensation," *Nonlinear Dyn.*, vol. 92, no. 4, pp. 1619–1635, Jun. 2018.

[4] J. Tao, Q. L. Sun, P. L. Tan, Z. Q. Chen, and Y. P. He, "Autonomous homing control of a powered parafoil with insufficient altitude," *ISA Trans.*, vol. 65, pp. 516–524, Nov. 2016.

[5] P. L. Tan, Q. L. Sun, E. L. Zhu, and Z. Q. Chen, "Active disturbance rejection control design for trajectory tracking of parafoil and payload system," *J. Comput.*, vol. 27, no. 2, pp. 59–66, 2016.

[6] N. Slegers, A. Brown, and J. Rogers, "Experimental investigation of stochastic parafoil guidance using a graphics processing unit," *Control Eng. Pract.*, vol. 36, pp. 27–38, Mar. 2015.

[7] P. L. Tan, Q. L. Sun, and Y. X. Jiang, "Characteristic model-based generalized predictive control and its application to the parafoil and payload system," *Optim. Control Appl. Methods*, vol. 40, no. 4, pp. 659–675, 2019.

[8] V. Devalla, A. K. Mondal, A. J. Arun Jeya Prakash, M. Prateek, and O. Prakash, "Guidance, navigation and control of a powered parafoil aerial vehicle," *Current Sci.*, vol. 111, no. 6, pp. 1045–1054, Mar. 2017.

[9] M. Watanabe and Y. Ochi, "Linear model of a powered paraglider and observer design," in *Proc. Int. Conf. Instrum., Control Inf. Technol.*, Tokyo, Japan, Aug. 2008, pp. 2135–2140.

[10] N. Slegers and M. Costello, "Model predictive control of a parafoil and payload system," *J. Guid., Control, Dyn.*, vol. 28, no. 4, pp. 816–821, Jul. 2005.

[11] H. Sun, Q. L. Sun, W. N. Wu, S. Z. Luo, and J. Tao, "Flexible modelling and altitude control for powered parafoil system based on active disturbance rejection control," *Int. J. Syst. Sci.*, vol. 50, no. 12, pp. 2385–2408, Sep. 2019.

[12] H. Sun, Q. L. Sun, J. Tao, S. Z. Luo, and Z. Q. Chen, "A hybrid control approach for powered parafoil combining active disturbance rejection control and unbalanced load compensation," *Proc. Inst. Mech. Eng. I, J. Syst. Control Eng.*, vol. 232, no. 3, pp. 299–314, Mar. 2018.

[13] P. L. Tan, Q. L. Sun, and Z. Q. Chen, "Application of active disturbance rejection control in trajectory tracking of powered parafoil system," *J. Zhejiang Univ. (Eng. Sci.)*, vol. 51, no. 5, pp. 992–999, 2016.

[14] P. L. Tan, S. Z. Luo, and Q. L. Sun, "Control strategy of power parafoil system based on coupling compensation," *Trans. Beijing Inst. Technol.*, vol. 39, no. 4, pp. 378–383, 2019.

[15] J. Tao, M. Dehmer, G. Xie, and Q. Zhou, "A generalized predictive control-based path following method for parafoil systems in wind environments," *IEEE Access*, vol. 7, pp. 42586–42595, 2019.

[16] N. Slegers, J. Kyle, and M. Costello, "Nonlinear model predictive control technique for unmanned air vehicles," *J. Guid., Control, Dyn.*, vol. 29, no. 5, pp. 1179–1188, Sep. 2006.

[17] N. Slegers and O. A. Yakimenko, "Optimal control for terminal guidance of autonomous parafoils," in *Proc. 20th AIAA Aerodyn. Decelerator Syst. Technol. Conf. Seminar*, Seattle, Washington, USA, 2009, p. 2958.

[18] H. Yang, L. Song, W. J. Wang, and J. Huang, "4-DOF longitudinal dynamic simulation of powered-parafoil," *J. Beijing Univ. Aeronaut. Astronaut.*, vol. 40, no. 11, pp. 1615–1622, 2014.

[19] Y. Gang, "Nine-degree of freedom modeling and flight dynamic analysis of parafoil aerial delivery system," in *Proc. Asia–Pacific Int. Symp. Aerosp. Technol.*, vol. 99, Sep. 2014, pp. 866–872.

[20] E. Mooij, Q. G. J. Wijnands, and B. Schat, "9 DoF parafoil/payload simulator development and validation," in *Proc. AIAA Modeling Simulation Technol. Conf. Exhibit*, Austin, Texas, USA, 2003, p. 5459.

[21] R. Guo, Q. B. Zhang, and Z. W. Feng, "Dynamic modeling and simulation of powered parafoil airdrop process," in *Proc. 5th Int. Conf. Mech., Automot. Mater. Eng. (CMAME)*, Guangzhou, China, 2017, pp. 234–239.

[22] S. Muller, O. Wagner, and G. Sachs, "A high-fidelity nonlinear multibody simulation model for parafoil systems," in *Proc. 17th AIAA Aerodyn. Decelerator Syst. Technol. Conf. Seminar*, Monterey, CA, USA, 2003, p. 2120.

[23] S. McCann, W. S. Ricci, T. Wendt, B. Brocato, and R. Benney, "Leaflet delivery system," in *Proc. 17th AIAA Aerodyn. Decelerator Syst. Technol. Conf. Seminar*, Monterey, CA, USA, 2003, p. 2139.

[24] C. Redelinghuys, "A flight simulation algorithm for a parafoil suspending an air vehicle," *J. Guid., Control, Dyn.*, vol. 30, no. 3, pp. 791–803, May 2007.

[25] M. Watanabe and Y. Ochi, "Modeling and simulation of nonlinear dynamics of a powered paraglider," in *Proc. AIAA Guid., Navigat. Control Conf. Exhibit*, Honolulu, HI, USA, 2008, p. 7418.

[26] E. L. Zhu, Q. L. Sun, P. L. Tan, Z. Q. Chen, X. F. Kang, and Y. P. He, "Modeling of powered parafoil based on Kirchhoff motion equation," *Nonlinear Dyn.*, vol. 79, no. 1, pp. 617–629, Jan. 2015.

PANLONG TAN received the B.S. and M.S. degrees in automation and control theory and control engineering from the Tianjin University of Technology, Tianjin, China, in 2010 and 2013, respectively, and the Ph.D. degree in control science and engineering from Nankai University, Tianjin, in 2016. He is currently a Postdoctoral Researcher with the College of Artificial Intelligence, Nankai University. His current research interests include the active disturbance rejection control and modeling and control of flexible spacecraft.

MINGWEI SUN received the B.S. degree in traffic signal and control from Northern Jiaotong University, Beijing, China, in 1995, and the Ph.D. degree in control theory and control engineering from Nankai University, Tianjin, China, in 2000.

From 2000 to 2008, he was a Flight Control Engineer with the Beijing Electro-mechanical Engineering Research Institute, Beijing. Since 2009, he has been with Nankai University, where he is currently a Professor with the College of Artificial Intelligence. His research interests include flight control, guidance, model predictive control, active disturbance rejection control, and nonlinear optimization.

QINGLIN SUN received the B.S. and M.S. degrees in control theory and control engineering from Tianjin University, Tianjin, China, in 1985 and 1990, respectively, and the Ph.D. degree in control science and engineering from Nankai University, Tianjin, China, in 2003.

He is currently a Professor with the College of Artificial Intelligence, Nankai University. He has published more than 100 peer-reviewed articles. His research interests include adaptive control, modeling and control of flexible spacecraft, complex systems, and embedded control systems and their applications.

ZENGQIANG CHEN received the B.S. degree in mathematics and the M.S. and Ph.D. degrees in control theory and control engineering from Nankai University, Tianjin, China, in 1987, 1990, and 1997, respectively.

Since 1990, he has been with Nankai University, where he is currently a Professor with the College of Artificial Intelligence. He has authored or coauthored more than 200 journal articles in his main areas of research, which are adaptive control, predictive control, intelligent control, and nonlinear control.